Optimal Rebinning of Time-of-Flight PET Data

Sangtae Ahn, IEEE[Member],
Signal and Image Processing Institute, University of Southern California, Los Angeles, CA 90089 USA

Sanghee Cho, IEEE[Member],
Signal and Image Processing Institute, University of Southern California, Los Angeles, CA 90089 USA. He is now with the Siemens Medical Solutions, Knoxville, TN 37932 USA

Quanzheng Li, IEEE[Member],
Signal and Image Processing Institute, University of Southern California, Los Angeles, CA 90089 USA

Yanguang Lin, IEEE[Student Member], and
Signal and Image Processing Institute, University of Southern California, Los Angeles, CA 90089 USA

Richard M. Leahy, IEEE[Fellow]
Signal and Image Processing Institute, University of Southern California, Los Angeles, CA 90089 USA

Richard M. Leahy: leahy@sipi.usc.edu

Abstract

Time-of-flight (TOF) positron emission tomography (PET) scanners offer the potential for significantly improved signal-to-noise ratio (SNR) and lesion detectability in clinical PET. However, fully 3D TOF PET image reconstruction is a challenging task due to the huge data size. One solution to this problem is to rebin TOF data into a lower dimensional format. We have recently developed Fourier rebinning methods for mapping TOF data into non-TOF formats that retain substantial SNR advantages relative to sinograms acquired without TOF information. However, mappings for rebinning into non-TOF formats are not unique and optimization of rebinning methods has not been widely investigated. In this paper we address the question of optimal rebinning in order to make full use of TOF information. We focus on FORET-3D, which approximately rebins 3D TOF data into 3D non-TOF sinogram formats without requiring a Fourier transform in the axial direction. We optimize the weighting for FORET-3D to minimize the variance, resulting in H^2-weighted FORET-3D, which turns out to be the best linear unbiased estimator (BLUE) under reasonable approximations and furthermore the uniformly minimum variance unbiased (UMVU) estimator under Gaussian noise assumptions. This implies that any information loss due to optimal rebinning is as a result only of the approximations used in deriving the rebinning equation and developing the optimal weighting. We demonstrate using simulated and real phantom TOF data that the optimal rebinning method achieves variance reduction and contrast recovery improvement compared to nonoptimized rebinning weightings. In our preliminary study using a simplified simulation setup, the performance of the optimal rebinning method was comparable to that of fully 3D TOF MAP.

Correspondence to: Richard M. Leahy, leahy@sipi.usc.edu.

Index Terms

Biomedical imaging; estimation; Fourier transforms; image reconstruction; positron emission tomography (PET)

I. INTRODUCTION

Time-Of-Flight (TOF) positron emission tomography (PET) scanners provide the potential for substantial signal-to-noise ratio (SNR) improvement [1]–[5] and better lesion detectability [6]. Therefore, TOF PET technology including scintillators, system hardware, and image reconstruction is attracting increasing interest [7]–[11]. However, fully 3D TOF PET image reconstruction is challenging due to the huge data sizes involved.

Analytical reconstruction for TOF PET based on a line-integral model was used in [2], [12]–[16]. In these methods, each TOF sinogram is backprojected with a 1D confidence weighting function that models uncertainty in the TOF measurement. Then an appropriate inverse filter is applied in the image space to reconstruct the tracer distribution. An alternative approach that reduces the computation cost is to rebin 3D TOF data into a lower dimensional space [16]. Single slice rebinning (SSRB-TOF) [17] combines the TOF oblique sinograms to form a set of stacked TOF direct sinograms in a similar manner to SSRB for non-TOF data [18]. As an alternative to SSRB-TOF, an approximate Fourier rebinning method mapping 3D TOF into 2D TOF data was proposed, where the rebinning is performed in the Fourier domain [19]. A similar approximate rebinning was also derived in the native coordinates of the TOF sinograms rather than the Fourier domain [20]. An exact rebinning equation was derived based on a consistency condition expressed by a partial differential equation in the continuous data domain, where rebinning is performed with respect to the axial variables [21], [22]. This result motivated the development of an approximate discrete axial rebinning method [21], [22]. We have previously developed an alternative exact rebinning method, which is based on a Fourier transform in the TOF variable, by using a generalized projection slice theorem [23].

All of the rebinning methods described above rebin 3D TOF to 2D TOF data and specifically retain the TOF component in the rebinned data. We have recently developed new rebinning methods that rebin 3D TOF to non-TOF data in either 3D or 2D forms and shown that rebinning into non-TOF sinograms retains significant SNR advantages over sinograms collected without TOF information [24]. These results include approximate rebinning methods that do not require estimation of missing data and we have shown that they have accuracy similar to that of Fourier rebinning for non-TOF data. These approximate rebinning methods can map all TOF bins for a single oblique sinogram into the corresponding oblique non-TOF sinogram with improved SNR relative to the non-TOF case and minimal approximation error.

Mappings that rebin into non-TOF formats are not unique and there exist infinitely many rebinnings, depending on which sinogram each TOF oblique sinogram is rebinned into and also depending on weights used in combining the rebinned data. It is important to optimize rebinning methods in order to make full use of TOF information and consequently to maximize the quality of images reconstructed from the rebinned data. In this paper we address the problem of finding an optimal method to rebin TOF data into non-TOF formats.

We focus on FORET-3D (FOurier REbinning of Time-of-flight data to 3D non-time-of-flight) [24], which rebins 3D TOF data into 3D non-TOF sinogram formats without requiring a Fourier transform in the axial direction and hence avoiding the missing data

problem [25], [26]. We formulate the rebinning problem as estimating 3D non-TOF sinograms from noisy 3D TOF data. The best linear unbiased estimator (BLUE) turns out to be a FORET-3D mapping with optimal weights, which is the uniformly minimum variance unbiased (UMVU) estimator if the noise is approximately Gaussian distributed for high SNR. This implies that any information loss due to optimal rebinning is as a result only of the approximations used in deriving the rebinning equation and developing the optimal weighting. The results in this paper were partly presented in [27].

II. BACKGROUND

A. Data Model

3D TOF data p from a cylindrical PET scanner can be modeled using line integrals along lines of response (LORs) weighted by a 1D TOF kernel H[19], [24]

$$p(s, \phi, z, \delta, t) = \sqrt{1+\delta^2} \int_{-\infty}^{\infty} h(t - l\sqrt{1+\delta^2}) \cdot f(s\cos\phi - l\sin\phi, s\sin\phi + l\cos\phi, z + l\delta) \mathrm{d}l \quad (1)$$

where $f \in \mathbb{R}^3$ denotes a 3D object; s, ϕ, z and δ specify each LOR, that is, s and ϕ are radial and angular coordinates, respectively, z represents the axial midpoint and δ is the tangent of the oblique angle; t is the TOF variable, which is the difference of the arrival times and converted to distance by multiplying by the speed of light (see Fig. 1). The TOF kernel is assumed to be shift invariant so that the integral in (1) is written in the form of a convolution. The expression for p in (1) is general enough to include 3D non-TOF data when $h(\cdot) = 1$; stacked 2D TOF sinograms when $\delta = 0$; and stacked 2D non-TOF sinograms when and $h(\cdot) = 1$ and $\delta = 0$. In this paper, 2D stacked sinograms are simply referred to as 2D data.

The TOF kernel models the uncertainty in TOF measurements. Here we use a Gaussian kernel [16], [28]–[30]

$$h(t) = \frac{1}{\sqrt{2\pi}\sigma_h} \exp\left(-\frac{t^2}{2\sigma_h^2}\right) \quad (2)$$

where $\sigma_h = \rho_h / \sqrt{8\log_e 2}$ with ρ_h being the full-width at half-maximum (FWHM) representing the timing resolution of the system (note that $h(\rho_H/2) = h(-\rho_H/2) = h(0)/2 = \max_t h(t)/2$). Since $H$is an even function, that is, $h(t) = h(-t)$, the following symmetry and periodicity property of p can be shown [19]: $p(s, \phi, z, \delta, t) = p(-s, \phi + \pi, z, -\delta, -t)$. Therefore, p is completely characterized once it is defined on the set $\mathbb{R} \times [0, \pi) \times \mathbb{R}^3$. Since $\int_{-\infty}^{\infty} h(t)\mathrm{d}t = 1$, the integral of the TOF data p over the TOF variable t yields non-TOF data.

Let $\mathcal{P}(\omega_s, \phi, z, \delta, \omega_t)$ be the 2D Fourier transform of $p(s, \phi, z, \delta, t)$ with respect to s and t where ω_s and ω_t are the frequency variables corresponding to s and t, respectively. The Fourier transformed data $\mathcal{P}$ represent 3D non-TOF data when $\omega_t = 0$ (recall that the DC component of TOF data in t is equivalent to non-TOF data), 2D TOF data when $\delta = 0$, and 2D non-TOF data when $\omega_t = 0$ and $\delta = 0$. Since $H$is an even function, a symmetry and periodicity property also holds for $\mathcal{P}$ such that $\mathcal{P}(\omega_s, \phi, z, \delta, \omega_t) = \mathcal{P}(-\omega_s, \phi, +\pi, z, -\delta, -\omega_t)$. We use the set $\mathbb{R}_+, \times [0, 2\pi) \times \mathbb{R}^3$, that is, $\omega_s \ge 0$, as the domain of $\mathcal{P}$ without loss of generality where $\mathbb{R}_+ = \{x \ge 0 : x \in \mathbb{R}\}$. Once $\mathcal{P}$ are defined on this set, function values elsewhere can be obtained using the symmetry and periodicity property.

B. Sinogram Rebinning Operator

We have previously derived an approximate rebinning equation, which maps a TOF oblique sinogram into a non-TOF oblique sinogram (where $\omega_t = 0$) in the Fourier domain [24]

$$\wp (\omega_s', \phi', z, \delta, 0) \approx \frac{\mathcal{H}(0)}{\mathcal{H}(\omega_t)} \wp (\omega_s, \phi, z, \delta, \omega_t) \tag{3}$$

for $\omega_s'^2 \geq \omega_t^2 (1+\delta^2)$ where

$$\omega_s = \sqrt{\omega_s'^2 - \omega_t^2 (1+\delta^2)} \tag{4}$$

$$\phi = \phi' - \arctan\left(\frac{\omega_t \sqrt{1+\delta^2}}{\omega_s} \right) \tag{5}$$

and $\mathcal{H}$ is the Fourier transform of h, that is

$$\mathcal{H}(\omega_t) = \exp\left(\frac{-\sigma_h^2 \omega_t^2}{2} \right) \tag{6}$$

which is real and positive. Equation (4) is slightly different from [24, Eq. (18)], since here we consider $\wp$ only on the domain $\omega_s \geq 0$. However, they are equivalent. In (5) and also throughout this paper, the value of the angular coordinate variable ϕ is considered to be wrapped so that it is constrained to $[0, 2\pi)$. Note that (3) does not require a Fourier transform in the axial variable z and thus there is no missing data problem.

The approximation error in (3) increases as $|\omega_t|$ and $|\delta|$ increase and $|\omega_s'|$ decreases [24]. When $\delta = 0$, the mapping (3) becomes exact between 2D TOF and 2D non-TOF sinograms [24]. The coordinate transformation (4) and (5), when $\omega_t \sqrt{1+\delta^2}$ is replaced with $\delta \omega_z$, is equivalent to that for the exact mapping between a non-TOF oblique and a non-TOF direct sinogram (cf. [24, (9)], and [25, (14)]). Fig. 2, which is a simplified version of [24, Fig. 3], shows a geometrical illustration of the coordinate transformation in (4) and (5). Mapping a TOF oblique sinogram $\wp_{z,\delta,\omega_t}(\omega_s, \phi)$ into a non-TOF oblique sinogram $\wp_{z,\delta}'(\omega_s', \phi')$, which is exact when $\delta = 0$, is equivalent to finding ω_s and ϕ given ω_s' and ϕ' as in the figure.

We define a sinogram rebinning operator, $\mathcal{R}_{\delta,\omega_t}$ which maps a TOF oblique sinogram $\wp_{z,\delta,\omega_t}(\omega_s, \phi) = \wp(\omega_s, \phi, z, \delta, \omega_t)$, into a non-TOF oblique sinogram $\wp_{z,\delta}'(\omega_s', \phi') = \wp'(\omega_s', \phi', z, \delta, 0)$, such that $\wp_{z,\delta}' = \mathcal{R}_{\delta,\omega_t} \wp_{z,\delta,\omega_t}$ implies

$$\wp_{z,\delta}' (\omega_s', \phi') = \begin{cases} \frac{\mathcal{H}(0)}{\mathcal{H}(\omega_t)} \wp_{z,\delta,\omega_t}(\omega_s, \phi), & \omega_s'^2 \geq \omega_t^2 (1+\delta^2) \\ 0, & \omega_s'^2 < \omega_t^2 (1+\delta^2) \end{cases} \tag{7}$$

where ω_s and ϕ are given in (4) and (5).

With the same approximation used in (3), an approximate inverse rebinning equation, which maps a non-TOF to a TOF oblique sinogram, can be derived [24]

$$\wp(\omega_s, \phi, z, \delta, \omega_t) \approx \frac{\mathcal{H}(\omega_t)}{\mathcal{H}(0)} \wp(\omega_s', \phi', z, \delta, 0) \tag{8}$$

where

$$\omega_s' = \sqrt{\omega_s^2 + \omega_t^2(1+\delta^2)} \tag{9}$$

$$\phi' = \phi + \arctan\left(\frac{\omega_t \sqrt{1+\delta^2}}{\omega_s}\right). \tag{10}$$

Using the mapping equation above, we define an inverse sinogram rebinning operator $\mathscr{T}_{\delta,\omega_t}$ such that $\wp_{z,\delta,\omega_t} = \mathscr{T}_{\delta,\omega_t}\wp_{z,\delta}'$ implies

$$\wp_{z,\delta,\omega_t}(\omega_s,\phi) = \frac{\mathscr{H}(\omega_t)}{\mathscr{H}(0)}\wp_{z,\delta}'(\omega_s',\phi') \tag{11}$$

where ω_s' and ϕ' are given in (9) and (10).

III. THEORY

A. FORET-3D

1) Continuous-Space Expression—We rebin TOF sinogram data into a low-dimensional non-TOF data format using the sinogram rebinning operator $\mathscr{R}_{\delta\omega_t}$. Since, for a fixed oblique plane parameterized by z and δ, multiple TOF oblique sinograms $\mathscr{P}_{z,\delta,\omega_t}$ for different ω_t's are rebinned into the non-TOF oblique sinogram format, it is natural to take an average of the rebinned sinograms over ω_t to estimate the non-TOF oblique sinogram

$$\hat{\wp}_{z,\delta}'(\omega_s',\phi') = \frac{\sum\limits_{\omega_t:\omega_s'^2\geq\chi^2}\alpha_{z,\delta,\omega_t}(\omega_s',\phi')(\mathscr{R}_{\delta,\omega_t}\wp_{z,\delta,\omega_t})(\omega_s',\phi')}{\sum\limits_{\omega_t:\omega_s'^2\geq\chi^2}\alpha_{z,\delta,\omega_t}(\omega_s',\phi')} \tag{12}$$

where $\chi = \omega_t\sqrt{1+\delta^2}$ and $\alpha_{z,\delta,\omega_t}$ is a nonnegative weight for each TOF sinogram.

How should we determine the weights? The simplest approach would be to take an unweighted average. We refer to the rebinning method with $\alpha_{z,\delta,\omega_t} = 1$ as "unweighted FORET-3D." However, this naive weighting approach performs even worse than using non-TOF sinograms acquired without TOF information, as shown in Section IV, for the following reason. The sinogram rebinning operator given in (7) includes a scaling factor $1/\mathscr{H}(\omega_t)$, which can be viewed as a high-pass filter since $\mathscr{H}$ is a low-pass filter. Therefore, noise is amplified where ω_t is large and $\mathscr{H}(\omega_t)$ is small. Although unweighted FORET-3D is far from optimal, we simply include it in the result section for comparison purposes.

To reduce this noise amplification, we have used $\alpha_{z,\delta,\omega_t}$ which is heuristically chosen to cancel out the scaling factor $1/\mathscr{H}(\omega_t)$ in the sinogram mapping operator (we inadvertently omitted a detailed description of using such weights in [24]). We refer to the rebinning method with $\alpha_{z,\delta,\omega_t} = \mathscr{H}(\omega_t)$ as "H-weighted FORET-3D." We have shown that H-weighted FORET-3D achieves significant SNR improvements over non-TOF data acquisition [24]. However, the heuristic weights are not optimal.

Suppose that the noise in the measured TOF sinogram $\mathscr{P}_{z,\delta\omega_t}$ is uncorrelated and identically distributed. This is a reasonable assumption as will be shown in Section III-C2. Then the

variance of the non-TOF sinogram $\wp'_{z,\delta}$ obtained by (7) will be proportional to $1/\mathcal{H}^2(\omega_t)$ if we ignore the coordinate transformation. It can be shown by the Gauss–Markov theorem [31, p.296], that a weight $\alpha_{z,\delta,\omega_t} = \mathcal{H}^2(\omega_t)$, inversely proportional to the variance, will result in the minimum variance of the weighted average. We call the rebinning method with $\alpha_{z,\delta,\omega_t} = \mathcal{H}^2(\omega_t)$ " H^2-weighted FORET-3D."

However, weighted averaging in (12) is not the only way to map 3D TOF data into 3D non-TOF data. Therefore, it is not clear whether H^2-weighted FORET-3D yields the minimum variance, even approximately, at least among linear unbiased estimators of the 3D non-TOF sinogram. The goal of this paper is to show that H^2-weighted FORET-3D is indeed the best linear unbiased estimator (BLUE). We will also identify necessary approximations and assumptions for the optimality of H^2-weighted FORET-3D and validate them.

2) Discretized FORET-3D—Here we focus on discretized models and rewrite FORET-3D mapping equations in vector-matrix forms. Let a vector $p^{ij}_{k'} \in \mathbf{C}^{N_s N_\phi}$ represent a discrete version of a TOF oblique sinogram $\mathcal{P}_{z,\delta,\omega_t}$ for $i = 0, \ldots, N_\delta - 1$, $j = 0, \ldots, N_z - 1$, and $k' = 0, \ldots, N_t - 1$ where i, j, and k' denote an oblique angle index for δ, an axial coordinate index for z and a TOF frequency variable index for ω_t, respectively, and N_s, N_ϕ, N_z, N_δ, and N_t are the number of sample points through the radial (s or ω_s), angular (ϕ), axial (z), oblique angle (δ), and TOF variable (t or ω_t) direction, respectively. For notational simplicity we assume we do not use zero padding for fast Fourier transforms (FFT) and the number of sample points in the Fourier and the original domain are the same without loss of generality; in practice we use a zero-padding factor of 2 when computing FFTs. Let $y^{ij}_{k'} \in \mathbf{C}^{N_s N_\phi}$ be a noisy TOF oblique sinogram such that

$$y^{ij}_{k'} = p^{ij}_{k'} + e^{ij}_{k'} \tag{13}$$

where $e^{ij}_{k'} \in \mathbf{C}^{N_s N_\phi}$ represents noise, which is zero-mean.

Suppose $k'_0 \triangleq 0$ corresponds to $\omega_t = 0$ and $p^{ij}_{k'_0}$ represents a non-TOF oblique sinogram. An estimate of $p^{ij}_{k'_0}$ obtained using unweighted FORET-3D (Section III-A1) can be written as

$$\hat{p}^{ij}_{k'_0} = \left(\sum_{k'=0}^{N_t-1} D^i_{k'} \right)^{-1} \sum_{k'=0}^{N_t-1} R^i_{k'} y^{ij}_{k'} \tag{14}$$

where the $N_s N_\phi \times N_s N_\phi$ matrix $R^i_{k'}$ is a discrete version of the approximate sinogram rebinning operator $\mathcal{R}_{\delta,\omega_t}$ defined in (7) and $D^i_{k'}$ is a diagonal matrix whose lth diagonal element is 1 if the ω'_s corresponding to the lth row of $R^i_{k'}$ satisfies $\omega'^2_s \geq \omega^2_t(1+\delta^2)$ and is 0 otherwise. Note that the lth diagonal element of $\sum_{k'=0}^{N_t-1} D^i_{k'}$ is the number of sample points through ω_t such that $\omega'^2_s \geq \omega^2_t(1+\delta^2)$ for given ω'_s and δ corresponding to index l and i, respectively. Similarly, H-weighted FORET-3D and H^2-weighted FORET-3D can be written as

$$\hat{p}^{ij}_{k'_0} = \left(\sum_{k'=0}^{N_t-1} H_{k'} D^i_{k'} \right)^{-1} \sum_{k'=0}^{N_t-1} H_{k'} R^i_{k'} y^{ij}_{k'} \tag{15}$$

and

$$\hat{p}_{k_0'}^{ij} = \left(\sum_{k'=0}^{N_t-1} H_{k'}^2 D_{k'}^i \right)^{-1} \sum_{k'=0}^{N_t-1} H_{k'}^2 R_{k'}^i y_{k'}^{ij} \qquad (16)$$

respectively, where $H_{k'}$ denote samples of $\mathcal{H}$.

B. BLUE

Here we view the rebinning as an inverse problem to estimate non-TOF sinogram values from noisy TOF data. To solve the inverse problem, we need a forward model to map the non-TOF sinograms into the TOF data. We use the approximate inverse sinogram rebinning operator given in (8) as a forward model. A TOF oblique sinogram $p_{k'}^{ij}$ can be modeled as

$$p_{k'}^{ij} \approx T_{k'}^i + p_{k_0'}^{ij} \qquad (17)$$

where the $N_s N_\phi \times N_s N_\phi$ matrix $T_{k'}^i$ represents a discrete version of $\mathcal{T}_{\delta,\omega_t}$ defined in (11), and $p_{k_0'}^{ij}$ represents a non-TOF sinogram as defined previously.

Suppose the measured data $y_{k'}^{ij}$ are uncorrelated across i, j and k'. This is a reasonable approximation as shown in Section III-C. Then the best linear unbiased estimator (BLUE) [31, p.296] of $p_{k_0'}^{ij}$ is given by

$$\hat{p}_{k_0'}^{ij} = \left(\sum_{k'=0}^{N_t-1} (T_{k'}^i)^* \left(K_{k'}^{ij} \right)^{-1} T_{k'}^i \right)^{-1} \sum_{k'=0}^{N_t-1} (T_{k'}^i)^* \left(K_{k'}^{ij} \right)^{-1} y_{k'}^{ij} \qquad (18)$$

where * denotes the conjugate transpose and

$$K_{k'}^{ij} = \mathrm{Cov} \left\{ y_{k'}^{ij} \right\}. \qquad (19)$$

Note that BLUE does not require any assumption on the noise distribution. If the noise is Gaussian distributed, e.g., in a case of high SNR, then (18) becomes the uniformly minimum variance unbiased (UMVU) estimator [32].

C. Equivalence of H^2-Weighted FORET-3D and BLUE

Suppose the following approximations hold:

$$\left(T_{k'}^i \right)^* \approx H_{k'}^2 R_{k'}^i \qquad (20)$$

$$\left(T_{k'}^i \right)^* T_{k'}^i \approx H_{k'}^2 D_{k'}^i \qquad (21)$$

$$K_{k'}^{ij} \approx \sigma_{ij}^2 I_{N_s N_\phi} \qquad (22)$$

where $I_{N_s N_\phi}$ is an $N_s N_\phi \times N_s N_\phi$ identity matrix and σ_{ij} is a positive scalar, which will be defined below. Then (16) and (18) are equivalent. In other words, if the above

approximations are reasonable, H^2-weighted FORET-3D is equivalent to BLUE (and to UMVU if the Gaussian noise assumption is reasonable). This is the key result of this paper. Now we show the validity of (20)–(22).

1) Adjoint of Inverse Sinogram Rebinning Operator—To obtain insights about (20) and (21), we examine continuous-space analogs through the adjoint of the inverse sinogram rebinning operators. Interestingly, the adjoint $(\mathscr{T}_{\delta,\omega_t})^*$ of the inverse sinogram rebinning operator $\mathscr{T}_{\delta,\omega_t}$ turns out to be a diagonally weighted version of the corresponding sinogram rebinning operator $\mathscr{R}_{\delta,\omega_t}$, that is

$$(\mathscr{T}_{\delta,\omega_t})^* = \mathscr{W}_{\delta,\omega_t}\mathscr{R}_{\delta,\omega_t} \tag{23}$$

where a diagonal weighting operator $\mathscr{W}_{\delta,\omega_t}$ is defined such that $q = \mathscr{W}_{\delta,\omega_t}r$ implies

$$q(\omega_s', \phi') = \begin{cases} \left|\frac{\mathscr{H}(\omega_t)}{\mathscr{H}(0)}\right|^2 \frac{\omega_s'}{\sqrt{\omega_s'^2 - \omega_t^2(1+\delta^2)}}r(\omega_s', \phi') & \\ \qquad\qquad \text{for } \omega_s' \geq \sqrt{\omega_t^2(1+\delta^2)} & \\ \left|\frac{\mathscr{H}(\omega_t)}{\mathscr{H}(0)}\right|^2 \quad \text{for } \omega_s' < \sqrt{\omega_t^2(1+\delta^2)} & \end{cases}. \tag{24}$$

See Appendix A for derivation of (23) and (24). Since $(\mathscr{R}_{\delta,\omega_t}\wp)(\omega_s', \phi')=0$ when $\omega_s' < \sqrt{\omega_t^2(1+\delta^2)}$ for any $\wp$ by (7), the diagonal weights of $\mathscr{W}_{\delta,\omega_t}$ for $\omega_s' < \sqrt{\omega_t^2(1+\delta^2)}$ indeed do not matter in the sense that $((\mathscr{T}_{\delta,\omega_t})^*\wp)(\omega_s', \phi')$ is always 0 for $\omega_s' < \sqrt{\omega_t^2(1+\delta^2)}$ in (23) whatever values are assigned to those weights.

Noting that $\mathscr{H}(0) = 1$ (recall we assume $\int h(t)dt = 1$) and that δ is practically small and ω_t is small compared to ω_s [24], we make the following approximation:

$$(\mathscr{T}_{\delta,\omega_t})^* \approx |\mathscr{H}(\omega_t)|^2 \mathscr{R}_{\delta,\omega_t} \tag{25}$$

which is accurate when $\omega_s' < \sqrt{\omega_t^2(1+\delta^2)}$ or $\omega_s' \gg \sqrt{\omega_t^2(1+\delta^2)}$ [see (23) and (24)]. The approximation (25) makes the resultant estimator simple to implement and robust to modeling and interpolation errors. Although this approximation becomes inaccurate when ω_s' is larger than $\sqrt{\omega_t^2(1+\delta^2)}$ but not much larger, such a region is usually small (since $\sqrt{\omega_t^2(1+\delta^2)}$ is practically small) and the inaccuracy does not introduce any systematic bias but rather increases the variance.

On the other hand, one can derive from (4), (5), (7), and (9)–(11) that

$$\mathscr{R}_{\delta,\omega_t}\mathscr{T}_{\delta,\omega_t} = \mathscr{D}_{\delta,\omega_t} \tag{26}$$

where $\mathscr{D}_{\delta,\omega_t}$ is defined such that $q = \mathscr{D}_{\delta,\omega_t}r$ implies

$$q(\omega_s', \phi') = \begin{cases} r(\omega_s', \phi'), & \omega_s' \geq \sqrt{\omega_t^2(1+\delta^2)} \\ 0, & \text{otherwise.} \end{cases} \tag{27}$$

The diagonal matrix $\boldsymbol{D}_{k'}^{i}$ defined in Section III-A2 is a discretized version of $\mathscr{D}_{\delta,\omega_t}$. Combining (25) and (26) yields

$$(\mathscr{T}_{\delta,\omega_t})^* \mathscr{T}_{\delta,\omega_t} \approx |\mathscr{H}(\omega_t)|^2 \mathscr{D}_{\delta,\omega_t}. \tag{28}$$

From (25) and (28), one can see that (20) and (21) are reasonable approximations. By substituting the noiseless TOF data $p_{k'}^{ij} \approx T_k^i$, $p_{k_0'}^{ij}$ from (17) into $\boldsymbol{y}_{k'}^{\mathbf{ij}}$ in (14), (15), and (16) and then using a discretized version of (26), $\boldsymbol{R}_{k'}^{i} \boldsymbol{T}_{k'}^{i} \approx \boldsymbol{D}_{k'}^{i}$, one can also see that $\hat{\boldsymbol{p}}_{k_0'}^{ij} \approx \boldsymbol{p}_{k_0'}^{ij}$, that is, FORET-3D is approximately unbiased.

2) Noise Model—Here we show that (22) is a reasonable approximation. Suppose we measure noisy TOF data z_{klm}^{ij}, a noisy discretized version of $p(s, \phi, z, \delta, t)$, where i represents an index for the oblique angle δ, j for the axial coordinate z, k for the TOF variable t, l for the radial coordinate s, and m for the transaxial angular coordinate ϕ. We take the 2D FFT of z_{klm}^{ij} with respect to k and l to obtain $y_{k'l'm}^{ij}$, a noisy discretized version of $\mathscr{P}_{z,\delta,\omega_t}(\omega_s, \phi)$, where k' represents an index for ω_t and l' for ω_s. Note $y_{k'l'm}^{ij}$ are the elements of $\boldsymbol{y}_{k'}^{ij}$ given in (13).

It is a reasonable assumption that the data z_{klm}^{ij} are independent with $\mathrm{Var}\left\{z_{klm}^{ij}\right\} = \sigma_{ijklm}^2$. Due to the independence of z_{klm}^{ij}, one can show that

$$\mathrm{Cov}\left\{y_{k'l'm}^{ij}, y_{p'q'r}^{uv}\right\} = C_m^{ij}(k'-p', l'-q')\delta_{iu}\delta_{jv}\delta_{mr} \tag{29}$$

where $C_m^{ij}(k', l')$ is the FFT of σ_{ijklm}^2 with respect to k and l, and $\delta_{..}$ is the Kronecker delta (see Appendix B for derivation). Note $C_m^{ij}(0, 0) = \sum_{k=0}^{N_t-1} \sum_{l=0}^{N_s-1} \sigma_{ijklm}^2 \triangleq \sigma_{ijm}^2$. The $y_{k'l'm}^{ij}$ are correlated across the TOF frequency variable index k' and the radial frequency index l'. In other words, $C_m^{ij}(k', l')$ is not simply an impulse at $(k', l') = (0, 0)$. However, practically, C_m^{ij} has a peak, centered at $(0, 0)$, with a relatively narrow width; see Fig. 3(a) for an illustration using realistically simulated data. Therefore, we approximate C_m^{ij} as an impulse:

$C_m^{ij}(k', l') \approx \sigma_{ijm}^2 \delta_{k'0} \delta_{l'0}$. We further approximate $\sigma_{ijm}^2 \approx \sigma_{ij}^2 \triangleq (1/N_\phi) \sum_{v=1}^{N_\phi} \sigma_{ijv}^2$ since σ_{ijm}^2 does not vary substantially with the transaxial angular index m in each oblique plane; see Fig. 3(b) for illustration. In summary, our noise covariance model is

$$\mathrm{Cov}\left\{y_{k'l'm}^{ij}, y_{p'q'r}^{uv}\right\} \approx \sigma_{ij}^2 \delta_{iu} \delta_{jv} \delta_{k'p'} \delta_{l'q'} \delta_{mr} \tag{30}$$

and therefore (22) follows.

D. Noise Properties of Rebinned Data

We now examine the noise properties of the rebinned data. It is important to know the covariance of the rebinned data for optimized image reconstruction. Although the approximations we make here for analysis may be oversimplifying, we can obtain useful insights through the analysis, estimates of SNR gains for the rebinning methods, and ideas of how to reconstruct images from rebinned data.

First, we approximate the inverse rebinning matrix: $T_{k'}^i \approx H_{k'} I_{N_s N_\phi}$. Considering that δ is generally small in practice and ω_t is usually smaller than ω_s [24], one can see from (9) and (10) that $\omega_s' \approx \omega_s$ and $\phi' \approx \phi$ and $\phi' \approx \phi$ is a useful, if crude, approximation for analysis purposes. For example, for the clinical PET scanner we simulate in Section IV, the maximum δ^2, ω_t and ω_s values are 0.068, 0.012/mm and 0.25/mm, respectively. Similarly, we approximate the rebinning matrix: $R_{k'}^i \approx (1/H_{k'}) I_{N_s N_\phi}$. Note this simplified rebinning is similar to single slice rebinning (SSRB) [17], [18] but collapses the TOF variable rather than the oblique angle.

Under those approximations, we can calculate the covariance matrix of the rebinned data $\hat{p}_{k_0'}^{ij}$ in (16) for H^2-weighted FORET-3D, ignoring D_k^i terms for simplicity

$$\mathrm{Cov}\left\{\hat{p}_{k_0'}^{ij}\right\} \approx \frac{1}{\left(\sum_{k'=0}^{N_t-1} H_{k'}^2\right)^2} \sum_{k'=0}^{N_t-1} \mathrm{Cov}\left\{H_{k'} y_{k'}^{ij}\right\} = \frac{1}{\left(\sum_{k'=0}^{N_t-1} H_{k'}^2\right)^2} \sum_{k'=0}^{N_t-1} H_{k'}^2 K_{k'}^{ij} = \frac{1}{\sum_{k'=0}^{N_t-1} H_{k'}^2} K_{k_0'}^{ij}$$

where (22) is used. Since $K_{k_0'}^{ij}$ is the covariance matrix of the non-TOF data $y_{k_0'}^{ij}$, the above equation implies that the rebinned data has approximately the same covariance matrix as the non-TOF data within the scaling factor $1/\sum_{k'=0}^{N_t-1} H_{k'}^2$. Therefore, $G_{H^2} \triangleq \sum_{k'=0}^{N_t-1} H_{k'}^2$ provides an estimate of the SNR gain for H^2-weighted FORET-3D compared to using non-TOF data acquired without TOF information.

Similarly, one can obtain

$$\mathrm{Cov}\left\{\hat{p}_{k_0'}^{ij}\right\} \approx \frac{N_t}{\left(\sum_{k'=0}^{N_t-1} H_{k'}\right)^2} K_{k_0'}^{ij}$$

using (15) for H-weighted FORET-3D, and

$$\mathrm{Cov}\left\{\hat{p}_{k_0'}^{ij}\right\} \approx \frac{\sum_{k'=0}^{N_t-1} \left(\frac{1}{H_{k'}^2}\right)}{N_t^2} K_{k_0'}^{ij}$$

using (14) for unweighted FORET-3D. Therefore, the SNR gain for H-weighted FORET-3D and for unweighted FORET-3D are given by

$G_H \triangleq \left(\sum_{k'=0}^{N_t-1} H_{k'}\right)^2 / N_t$ and $G_{no} \triangleq N_t^2 / \left(\sum_{k'=0}^{N_t-1} (1/H_{k'}^2)\right)$, respectively. One can arithmetically show that $G_{H^2} \geq G_H \geq G_{no}$ where equality holds only if $H_0 = \cdots = H_{N_t-1}$, which corresponds to $h(t) = \delta(t)$ when there is no uncertainty in the TOF measurement.

We can further examine the SNR gains for FORET-3D by exploiting the Gaussianity of the TOF kernel. Ignoring aliasing and windowing effects [33], one can calculate, from (2), $\sum_{k'=0}^{N_t-1} H_{k'} \approx h(0) N_t \Delta t = N_t \Delta t / (\sqrt{2\pi} \sigma_h) = \sqrt{4 \log_e 2/\pi} (N_t \Delta t / \rho_h)$ where Δt is the sampling interval in the TOF variable t direction. Since squaring $\mathcal{H}$ is equivalent to multiplying σ_h by

$\sqrt{2}$ [see (6)], one can also calculate $\sum_{k'=0}^{N_t-1} H_{k'}^2 \approx N_t \Delta t/(2\sqrt{\pi}\sigma_h) = \sqrt{2\log_e 2/\pi}(N_t\Delta t/\rho_h)$. Using these, we have

$$G_{H^2} \approx \sqrt{\frac{2\log_e 2}{\pi}\frac{N_t\Delta t}{\rho_h}} \tag{31}$$

$$G_H \approx \frac{4\log_e 2}{\pi}\frac{N_t(\Delta t)^2}{\rho_h^2} = G_{H^2}\sqrt{\frac{8\log_e 2}{\pi}\frac{\Delta t}{\rho_h}}. \tag{32}$$

We take the sampling interval Δt for the TOF variable as half the timing resolution ρ_h, that is, $\Delta t = \rho_h/2$. In this case, the aliasing error is negligible [23], and the SNR gains become and $G_{H^2} \approx 0.332 N_t$ and $G_H \approx 0.221 N_t \approx 0.664 G_{H^2}$. Since we assume we have already corrected for scatter and randoms, our uncorrelated noise model requires that the TOF kernel along each LOR should overlap with the object and therefore $N_t\Delta t$ should be about the object size; if a TOF kernel along an LOR does not overlap with the object, the corresponding data would be deterministically zero-valued. The SNR gain achieved by the optimal H^2-weighted FORET-3D is proportional to the number of TOF bins overlapping with the object, and the optimal gain is larger than that for H-weighted FORET-3D by about 30%.

Interestingly, if $N_t\Delta t$ in (31) is replaced with the diameter of a disk object, G_{H^2} is identical to Tomitani's expression for the SNR gain of confidence weighted filtered backprojection (FBP) using TOF data [12]. Tomitani's expression was also shown to provide reasonably accurate estimates of the SNR gain achieved using the full TOF data in statistical image reconstruction when the object is much larger than the timing resolution [34]. This implies that our optimal rebinning method, H^2-weighted FORET-3D, could approach fully 3D TOF reconstruction in terms of noise variance while achieving substantial reduction of computation.

E. Image Reconstruction From Rebinned Data

As shown in Section III-D, the covariance of the rebinned data is approximately equal, within a scale factor, to the covariance of the non-TOF data acquired without TOF information. Since the non-TOF data are independent, the rebinned data are also nearly independent, as demonstrated in Section IV. If the non-TOF data follow the Poisson distribution, then the variance of the rebinned data will be approximately proportional to its mean. However, before applying rebinning methods, the measured data should be corrected for detector efficiency, attenuation and scatter and randoms since the rebinning methods are based on line integral based projection models. Data correction destroys the Poisson distribution and the variance of corrected data is no longer proportional to its mean.

Although data must first be corrected before rebinning, we can then undo the correction by dividing the rebinned data by the correction factors as in [35]. One can show that the rebinned data after undoing correction have approximately the same covariance structure as the raw non-TOF data before data correction, within the SNR gain scaling factor (see Appendix B). Since the non-TOF data before data correction follow the independent Poisson distribution, the variance of the rebinned data after undoing correction is approximately proportional to its mean and the rebinned data are independent. This finding is similar to previous observations for rebinning of non-TOF data, which were used to justify use of EM or OSEM reconstruction of Fourier rebinned data after undoing corrections [35].

Therefore, one can use penalized weighted least squares (PWLS) [36] for reconstructing images from the rebinned data with diagonal weights, equal to the inverse of the variance of the rebinned data, which can be practically approximated from experimental data after rebinning in a manner similar to that described in [36]. Alternatively, it is a practically reasonable choice to reconstruct images from the rebinned data using Poisson based ML (maximum likelihood) orMAP (maximum *a posteriori*) estimation since the rebinned data is approximately Poisson distributed in the sense that the variance of the data is approximately proportional to the mean. In this case, one can use existing non-TOF data reconstruction codes without modification, which avoids the need to estimate the weights for PWLS. In Section IV, we apply MAP reconstruction methods to simulated and real TOF data.

IV. RESULTS

A. 3D TOF PET Simulation

1) Simulation Setup—To evaluate the performance of the optimal rebinning method, we simulated the Siemens Biograph PET/CT TruePoint TrueV scanner [37] as in [24]. The scanner had 672 detectors per ring and 55 rings with a ring radius of 421 mm and an axial field of view of 216 mm. We generated 3D TOF data using line integral based projectors [38] and a Gaussian TOF kernel [28] with timing resolution 500 ps, and the data were sampled with a sampling period of 250 ps, producing 15 TOF bins. The maximum ring difference was 54 and the number of LORs per angle was 336. We had 639 oblique and direct sinogram planes with span 11. The image size was $256 \times 256 \times 109$ with a voxel size of 2 mm.

The NCAT torso phantom was used as a 3D object for data generation [see Fig. 4(a)] [39]. We generated noisy 3D TOF data with a total of 20 M counts for trues and we simulated randoms corresponding to a uniform field of 15% of the total count. We simulated Poisson noise and produced randoms-precorrected data, simulating real-time randoms subtraction [40]. Scatter, attenuation and detector efficiencies were not considered for simplicity. As long as the data is properly corrected, correction factors such as randoms, scatter, attenuation and normalization do not affect the rebinning methods other than through increased variance, which we achieve through use of simulated randoms only. The effects of inaccurate correction on the rebinning methods are not investigated in this paper.

Noisy 3D TOF data were rebinned into 3D non-TOF data by FORET-3D with the three different weightings given in (14), (15), and (16). To reduce approximation errors, for small $|\omega_s|$, only the data for small $|\omega_t|$ were used for rebinning. As in [24], when the index for $|\omega_s|$ was less than 7, we only rebinned the data corresponding to $|\omega_t| = 0$. The 3D non-TOF sinograms acquired without TOF information were obtained by summing the 3D TOF data over the TOF bins.

A fully 3D MAP reconstruction method [41] was applied to the rebinned data and also to the non-TOF data acquired without TOF information. For each reconstruction, two iterations of OSEM (ordered subsets expectation maximization) with six subsets [42] followed by 30 iterations of PCG (preconditioned conjugate gradient) were performed. We have implemented fully 3D TOF MAP by modifying our non-TOF MAP code and applied it to TOF data. For each reconstruction, we ran 10–15 iterations of PCG, which were reasonable for practical convergence. Note that convergence rates for TOF reconstruction are faster than non-TOF because of TOF reconstruction being better conditioned.

2) Comparison of Rebinned Data—To evaluate the performance of FORET-3D with different weights, we compared the rebinned data and also the non-TOF data using a Monte Carlo simulation with 50 noisy data sets.

Fig. 4(b) shows the profiles of the sample mean for the rebinned data in an axial center plane with the maximum ring difference. The mean profiles for FORET-3D agreed well with that for the non-TOF data acquired without TOF information. This implies that FORET-3D is nearly free of systematic bias as discussed in Section III-C1.

Fig. 4(c) shows the profiles of the sample variance for the rebinned data. Unweighted FORET-3D showed even larger variance than the non-TOF data acquired without TOF information. However, using H-weights and H^2-weights substantially reduced the variance and the optimal H^2-weighted FORET-3D gave the smallest variance.

To further investigate the SNR gain of the rebinning methods compared to the non-TOF data acquired without TOF information, we calculated the ratios of the variance of the non-TOF data and the rebinned data in all sinogram bins. Fig. 5(a)–(c) shows the histograms of the variance ratios. The median ratio for H^2-weighted FORET-3D was 6.1, meaning that the variance of the rebinned data is smaller than that of the non-TOF data by a factor of about 6.1 [Fig. 5(a)]. The median ratio is close to the estimated SNR gain factor $G_{H^2} \approx 0.332 \times 15 = 5.0$ (see Section III-D) although that calculation was based on a very simplified model. The median ratio for H-weighted FORET-3D was 4.7 [Fig. 5(b)] while the estimated SNR gain factor was $G_H \approx 0.221 \times 15 = 3.3$ (see Section III-D). The median ratio for unweighted FORET-3D was 0.36, meaning the variance for unweighted FORET-3D is about three times that for the non-TOF data.

The difference between H-weighted and H^2-weighted FORET-3D in log-scaled variance profiles in Fig. 4(c) did not seem large but the mean ratio of H-weighted to H^2-weighted FORET-3D was 1.30 [Fig. 5(d)]. This implies optimal H^2-weighted FORET-3D has a better SNR than H-weighted FORET-3D by about 30%, which agrees with the analysis results in Section III-D.

As can be seen in Fig. 4(c), the shapes of the variance profiles for FORET-3D look similar to that for the non-TOF data acquired without TOF information. The variance of H^2-weighted FORET-3D was highly correlated with that of the non-TOF data across sinogram bins (Pearson correlation coefficient = 0.9265). Also, the correlation coefficient between the variance of H-weighted FORET-3D and the non-TOF data was 0.8935, and the correlation coefficient was 0.8719 for unweighted FORET-3D. The variance of the rebinned data was nearly a scaled version of that of the non-TOF data, which agrees with the analysis results in Section III-D. We also calculated the covariance of the rebinned data to test whether there is a spatial correlation in the rebinned data. Fig. 4(d) shows profiles of the covariance between the sinogram central bin and all the sinogram bins in the central oblique plane with the maximum ring difference. The spatial correlation in the rebinned data is small and it is practically reasonable to assume the rebinned data are spatially uncorrelated.

3) Monte Carlo Simulation for 3D Data Reconstruction—We conducted a Monte Carlo simulation study using 50 noisy 3D TOF data sets to evaluate and compare the statistical properties of reconstructed images at two ROIs in the center plane [ROI A and B in Fig. 4(a)]. For each noisy TOF data set, we performed fully 3D TOF MAP reconstruction using quadratic regularization with smoothing parameters spatially variant to achieve count-invariant resolution [43]. We rebinned each TOF data set by H-weighted and H^2-weighted FORET-3D and also obtained a noisy non-TOF data set by summing the TOF data over TOF bins, and then applied fully 3D non-TOF MAP [41] to the rebinned and the non-TOF data with varying smoothing parameters.

To make a fair comparison of the noise properties of different methods, for each ROI, we applied 2D Gaussian smoothing so that the following recovery coefficient (RC), which is the normalized sample mean of ROI quantitation, is matched for different methods

$$\text{RC} = \frac{\frac{1}{N}\sum_k \sum_{j\in\text{ROI}} \hat{f}^k_j}{\sum_{j\in\text{ROI}} f^{\text{true}}_j}$$

where $\hat{f}^k_j$ is the reconstructed value at voxel j for data set k, f^{true}_j is the true value at voxel j and N is the number of data sets. To quantify noise, we calculated a normalized standard deviation of ROI quantitation

$$\frac{\sqrt{\frac{1}{N-1}\sum_k \left(\sum_{j\in\text{ROI}} \hat{f}^k_j - \frac{1}{N}\sum_{k'} \sum_{j'\in\text{ROI}} \hat{f}^{k'}_{j'}\right)^2}}{\sum_{j\in\text{ROI}} f^{\text{true}}_j}.$$

We also estimated the voxel-wise variance as the sample variance across realizations averaged within ROI

$$\frac{1}{N_{\text{ROI}}}\sum_{j\in\text{ROI}} \frac{1}{N-1}\sum_k \left(\hat{f}^k_j - \frac{1}{N}\sum_{k'} \hat{f}^{k'}_j\right)^2$$

where N_{ROI} is the number of voxels in ROI.

Fig. 6(a) and (b) shows the trade-off between recovery coefficient and standard deviation of ROI quantitation. Fig. 6(c) and (d) shows the trade-off between ROI recovery coefficient and voxel-wise variance across realizations averaged within ROI. Standard errors were computed in all cases using bootstrap resampling. As can be seen in Fig. 6, between H^2-weighted and H-weighted FORET-3D and non-TOF data acquisition, H^2-weighted FORET-3D consistently produced the minimum statistical uncertainty at matched ROI recovery coefficient while non-TOF data acquisition produced the maximum statistical noise (see [27, Fig. 5], for a comparison of resolution and variance trade-offs). On the other hand, H^2-weighted FORET-3D and TOF MAP seemed comparable while the former occasionally outperformed the latter and vice versa. It should be noted that we observed spatially nonuniform voxel variance within ROI and also different spatial noise correlations for TOF MAP and H^2-weighted FORET-3D (not shown here). This explains, for example, why TOF MAP showed a higher standard deviation of ROI quantitation for ROI A than H^2-weighted FORET-3D for the low recovery coefficient [see the left-most marks in Fig. 6(a)] but showed a similar voxel variance averaged within ROI A [see the left-most marks in Fig. 6(c)]. Further investigation will be needed to evaluate more rigorously FORET-3D against TOF MAP as discussed in Section V. However, this preliminary study demonstrates that the performance of H^2-weighted FORET-3D is comparable to that of TOF MAP in our simplified simulation setup.

B. Application to Real Data in Phantom Study

We applied the rebinning methods to experimental TOF data obtained from a prototype TOF Siemens Biograph TruePoint TrueV PET/CT scanner by scanning a Data Spectrum

anthropomorphic torso phantom with a lesion and background activity ratio of 12:1. The scan time was 60 min and the number of total prompts amounted to 2.6×10^9. Total counts are high relative to average *in vivo* studies but the data set is sufficient to demonstrate the relative performance of the rebinning methods and non-TOF data acquisition since the processing performed here is all linear.

We reconstructed images from the rebinned data and also from the non-TOF data by a fully 3D MAP reconstruction method (see Fig. 7). To evaluate contrast recovery, we chose a transverse plane and took a background region-of-interest (ROI) as shown in Fig. 7 and a lesion ROI of 4×4 voxels to include a lesion around the center. The diameter of the lesion was 7.8 mm. We calculated a contrast-to-noise ratio (CNR) as

$$\text{CNR} = \frac{\frac{1}{N_l}\sum_{j \in \text{ROI}_l}\hat{f}_j - \frac{1}{N_b}\sum_{j \in \text{ROI}_b}\hat{f}_j}{\sqrt{\frac{1}{N_b - 1}\sum_{j \in \text{ROI}_b}\left(\hat{f}_j - \frac{1}{N_b}\sum_{j' \in \text{ROI}_b}\hat{f}_{j'}\right)^2}}$$

where $\hat{f}_j$ is the reconstructed value at voxel j, ROI_l the lesion ROI, ROI_b the background ROI, N_l the number of voxels in the lesion ROI and N_b the number of voxels in the background ROI. The CNR was 17.97 for H^2-weighted FORET-3D, 16.41 for H-weighted FORET-3D and 10.95 for non-TOF data acquisition. The optimal H^2-weighted FORET-3D yielded the largest CNR, with significant improvement compared to non-TOF data acquisition.

V. DISCUSSION

We have optimized a Fourier rebinning method, which rebins 3D TOF data into 3D non-TOF data formats, and derived H^2-weighted FORET-3D. This method does not require a Fourier transform in the axial direction and is therefore a practical method that does not suffer from a missing data problem. H^2-weighted FORET-3D is shown to be the BLUE (best linear unbiased estimator) of non-TOF sinograms under reasonable approximations and the UMVU (uniformly minimum variance unbiased) estimator under Gaussian noise assumptions. This implies that we lose little information as a result of optimal rebinning. The optimal rebinning method was applied to real phantom data as well as simulated data and showed clear SNR and contrast recovery improvements over the other rebinning weights and non-TOF data acquisition. Furthermore, the SNR gain achieved by the optimal rebinning was close to that predicted by Tomitani's expression [12], which was also confirmed in the context of likelihood-based image reconstruction using full TOF data [34]. This suggests that optimal rebinning should approach the performance of fully 3D TOF reconstruction, at least with respect to reconstructed image noise variance, while achieving substantial reductions in computation cost.

In our MC simulation study, H^2-weighted FORET-3D showed comparable performance to, and occasionally outperformed, fully 3D TOF MAP. This is unsurprising in that 3D TOF MAP reconstruction was not optimal for the data we generated, although it would not be far from optimal, because of randoms-precorrection, which destroys the Poisson statistics [40], and also model mismatch (a line integral based projector [38] used for data generation and the geometric projector [44] used for both TOF MAP and non-TOF MAP reconstruction). Nonetheless, the simulation results are promising, and further investigation will be needed to evaluate the performance of the rebinning methods against TOF MAP in more realistic studies, where correction factors such as attenuation and detector efficiency and detector blurring are considered, and also in clinical data.

The derivation of the optimal H^2-weighted FORET-3D is based on several approximations as summarized as follows. First, the sinogram rebinning operator $\mathcal{R}_{\delta,\omega_t}$ and the inverse operator $\mathcal{T}_{\delta,\omega_t}$ used for deriving FORET-3D, are approximate. Since the approximation error increases as $|\omega_t|$ increases and $|\omega_s|$ decreases, we used for small $|\omega_s|$ only the sinograms with small $|\omega_t|$, which is a common practice to reduce errors in approximate Fourier rebinning [24], [25]. This approach reduces systematic bias, possibly at the cost of increased variance. However, the increased variance may not be significant because the $\mathcal{H}^2(\omega_t)$ weight decreases as $|\omega_t|$ increases. Second, to show the weights for H^2-weighted FORET-3D are optimal, we made approximations related to the inverse sinogram rebinning operator in (20) and (21) and assumed an uncorrelated noise in the Fourier space. The approximations in (20) and (21) make the resulting estimator simple and robust to modeling and numerical errors

but become inaccurate when ω_s' is larger than $\sqrt{\omega_t^2(1+\delta^2)}$ but not much larger. Also, the noise model becomes inaccurate when the noise is correlated in the Fourier space. One such instance is when the object size is small and the noise covariance is radially narrow in sinogram space and broad in Fourier space. In this case, since the object is small compared to the timing resolution, TOF information is not very useful anyway. Note that suboptimality in the weights for FORET-3D that arise from any inaccurate approximations does not introduce any systematic bias but rather increases the variance. Finally, we assume the data have been corrected for randoms, scatter, attenuation and normalization before rebinning. The effects of any inaccuracy in the correction factors on rebinning results have not been examined in this paper.

Although we focus on FORET-3D, which rebins 3D TOF into 3D non-TOF data, the methods we present in this paper apply to other rebinning methods. Among them, probably the most interesting one would be FORET-2D, which rebins 3D TOF into 2D non-TOF data. Although our preliminary study in [24] shows the approximations error for FORET-2D seem somewhat larger than that for FORET-3D, it is worthwhile to further investigate the method since the computational saving for reconstruction would be substantial.

Acknowledgments

APPENDIX A

Here we derive the adjoint of $\mathcal{T}_{\delta,\omega_t}$. For any functions $q(\omega_s, \phi)$ and $r(\omega_s, \phi)$, we have

$$\langle q, \mathscr{T}_{\delta,\omega_t} r\rangle$$

$$= \int_0^\infty \int_0^{2\pi} q(\omega_s,$$

$$\phi)\left((\mathscr{T}_{\delta,\omega_t} r)(\omega_s,\phi)\right)^* d\phi d\omega_s$$

$$= \int_0^\infty \int_0^{2\pi} q(\omega_s,$$

$$\phi)\frac{\mathscr{H}^*(\omega_t)}{\mathscr{H}^*(0)} r^*(\omega_s',$$

$$\phi')\, d\phi d\omega_s \qquad (33)$$

$$= \left|\frac{\mathscr{H}(\omega_t)}{\mathscr{H}(0)}\right|^2 \int_0^\infty \int_0^{2\pi} \frac{\mathscr{H}(0)}{\mathscr{H}(\omega_t)} q(\omega_s,$$

$$\phi)r^*(\omega_s',$$

$$\phi')\, d\phi d\omega_s$$

$$= \left|\frac{\mathscr{H}(\omega_t)}{\mathscr{H}(0)}\right|^2 \int_\chi^\infty \int_0^{2\pi} (\mathscr{R}_{\delta,\omega_t} q)(\omega_s',\phi')\cdot r^*(\omega_s',$$

$$\phi')\left|\frac{\partial(\omega_s,\phi)}{\partial(\omega_s',\phi')}\right| d\phi' d\omega_s'$$

$$= \left|\frac{\mathscr{H}(\omega_t)}{\mathscr{H}(0)}\right|^2 \int_\chi^\infty \int_0^{2\pi} (\mathscr{R}_{\delta,\omega_t} q)(\omega_s',\phi')\cdot r^*(\omega_s',\phi')\frac{\omega_s'}{\sqrt{\omega_s'^2 - \chi^2}} d\phi' d\omega_s' \qquad (34)$$

where $\chi = \sqrt{\omega_t^2(1+\delta^2)}$, a change of variables is made in (33), and the Jacobian determinant $|\partial(\omega_s,\phi)/\partial(\omega_s',\phi')|$ is computed using (4) and (5). Since (34) equals $\rangle(\mathscr{T}_{\delta,\omega_t})^* q, r\langle$ by the definition of the adjoint operator, $(\mathscr{T}_{\delta,\omega_t})^*$ can be written as (23).

APPENDIX B

First, we prove (29) in Section III-C2. Suppose z_{klm}^{ij} are independent with covariance $\text{Cov}\{z_{klm}^{ij}, z_{pqr}^{uv}\} = \sigma_{ijklm}^2 \delta_{iu}\delta_{jv}\delta_{kp}\delta_{lq}\delta_{mr}$. Let $y_{k'l'm}^{ij}$ be the 2D FFT of z_{klm}^{ij} with respect to k and l. Then one can calculate the covariance of $y_{k'l'm}^{ij}$ and $y_{p'q'm}^{ij}$ as

$$\text{Cov}\left\{y_{k'l'm}^{ij},\right.$$

$$\left. y_{p'q'm}^{ij}\right\}$$

$$= \text{Cov}\left\{\sum_{k,l} z_{klm}^{ij} e^{-2\pi i(k'k/N_t + l'l/N_s)}, \sum_{p,q} z_{pqm}^{ij} e^{-2\pi i(p'p/N_t + q'q/N_s)}\right\}$$

$$= \sum_{k,l,p,q} e^{-2\pi i((k'k - p'p)/N_t + (l'l - q'q)/N_s)} \text{Cov}\left\{z_{klm}^{ij},\right. \qquad (35)$$

$$\left. z_{pqm}^{ij}\right\}$$

$$= \sum_{k,l} e^{-2\pi i((k'-p')k/N_t + (l'-q')l/N_s)} \sigma_{ijklm}^2$$

$$= C_m^{ij}(k'-p', l'-q')$$

where $C_m^{ij}(k', l')$ is the FFT of σ_{ijklm}^2 with respect to k and l. Since we deal with complex numbers in the Fourier domain, we adopt the definition of covariance, $\text{Cov}\{X, Y\} \triangleq E[(X - E[X])(Y - E[Y])^*]$ where $*$ denotes complex conjugate [45, p.66]. The sign change in (35) is due to this.

Next, we prove the claim made in Section III-E that the rebinned data after undoing correction have approximately the same covariance structure as the raw non-TOF data before data correction within a scaling factor. We consider corrected data $\tilde{z}_{klm}^{ij} = c_{ijlm} z_{klm}^{ij}$, which are statistically independent, where c_{ijklm} are multiplicative correction factors. Suppose that $\tilde{y}_{k'l'm}^{ij}$ is the FFT of $\tilde{z}_{klm}^{ij}$ with respect to k and l and that we apply FORET-3D, given in (14), (15) or (16), to the corrected data $\tilde{y}_{k'l'm}^{ij}$ and obtain rebinned data $\widehat{\tilde{p}}_{lm}^{ij}$ as an estimate of the non-TOF sinogram. Assume that the covariance of $\tilde{y}_{k'l'm}^{ij}$ follows (30). Then the covariance of the rebinned data is approximately the same as that of the non-TOF data $\tilde{z}_{lm}^{ij} \triangleq \sum_{k=0}^{N_t-1} \tilde{z}_{klm}^{ij}$ within a scaling factor $1/G$ where G is a SNR gain factor, as shown in Section III-D. Therefore, the rebinned data $\widehat{\tilde{p}}_{lm}^{ij}$ are approximately independent and the variance is given by

$$\text{var}\left\{\widehat{\tilde{p}}_{lm}^{ij}\right\} \approx (1/G)\text{var}\left\{\tilde{z}_{lm}^{ij}\right\} = (1/G)c_{ijlm}^2 \text{var}\left\{z_{lm}^{ij}\right\}$$ where $z_{lm}^{ij} \triangleq \sum_{k=0}^{N_t-1} z_{klm}^{ij} = \tilde{z}_{lm}^{ij}/c_{ijlm}$ denote the

non-TOF data before correction. Since $\text{var}\left\{\widehat{\tilde{p}}_{lm}^{ij}/c_{ijlm}\right\} \approx (1/G)\text{var}\left\{z_{lm}^{ij}\right\}$, the variance of the rebinned data after undoing the correction is a scaled version of the variance of the raw non-TOF data before correction.

References

1. Moses WW. Time of flight in PET revisited. IEEE Trans. Nucl. Sci. 2003 Oct.vol. 50(no. 5):1325–1330.

2. Conti M, Bendriem B, Casey M, Chen M, Kehren F, Michel C, Panin V. First experimental results of time-of-flight reconstruction on an LSOPET scanner. Phys. Med. Biol. 2005 Oct.vol. 50(no. 19): 4507–4526. [PubMed: 16177486]

3. Moses WW. Recent advances and future advances in time-of-flight PET. Nucl. Instrum. Meth. Phys. Res. A. 2007 Oct.vol. 580(no. 2):919–924.

4. Cherry SR. The 2006 Henry N. wagner lecture: Of mice and men (and positrons)—Advances in PET imaging technology. J. Nucl. Med. 2006 Nov.vol. 47(no. 11):1735–1745. [PubMed: 17079804]

5. Karp JS, Surti S, Daube-Witherspoon ME, Muehllehner G. Benefit of time-of-flight in PET: Experimental and clinical results. J. Nucl. Med. 2008 Mar.vol. 49(no. 3):462–470. [PubMed: 18287269]

6. Surti S, Karp JS. Experimental evaluation of a simple lesion detection task with time-of-flight PET. Phys. Med. Biol. 2009 Jan.vol. 54(no. 2):373–384. [PubMed: 19098351]

7. Lewellen TK. Time-of-flight PET. Seminars Nucl. Med. 1998 Jul.vol. 28(no. 3):268–275.

8. Surti S, Karp JS, Muehllehner G, Raby PS. Investigation of lanthanum scintillators for 3-D PET. IEEE Trans. Nucl. Sci. 2003 Jun.vol. 50(no. 3):348–354.

9. Surti S, Karp JS, Popescu LA, Daube-Witherspoon ME, Werner M. Investigation of time-of-flight benefit for fully 3-D PET. IEEE Trans. Med. Imag. 2006 May.vol. 25(no. 5):529–538.

10. Surti S, Kuhn A, Werner ME, Perkins AE, Kolthammer J, Karp JS. Performance of philips gemini TF PET/CT scanner with special consideration for its time-of-flight imaging capabilities. J. Nucl. Med. 2007 Mar.vol. 48(no. 3):471–480. [PubMed: 17332626]

11. Conti M. State of the art and challenges of time-of-flight PET. Physica Medica. 2009; vol. 25:1–11. [PubMed: 19101188]

12. Tomitani T. Image reconstruction and noise evaluation in photon time-of-flight assisted positron emission tomography. IEEE Trans. Nucl. Sci. 1981 Dec.vol. NS-28(no. 6):4582–4589.

13. Snyder DL, Thomas LJ, Ter-Pogossian MM. Amathematical model for positron-emission tomography systems having time-of-flight measurements. IEEE Trans. Nucl. Sci. 1981 Jun.vol. 28(no. 3):3575–3583.

14. Philippe EA, Mullani N, Wong W, Hartz R. Real-time image-reconstruction for time-of-flight positron emission tomography (TOFPET). IEEE Trans. Nucl. Sci. 1982 Feb.vol. 29(no. 1):524–528.

15. Mallon A, Grangeat P. 3-dimensional PET reconstruction with time-of-flight measurement. Phys. Med. Biol. 1992 Mar.vol. 37(no. 3):717–729. [PubMed: 1565699]

16. Vandenberghe S, Karp J. Rebinning and reconstruction techniques for 3D TOF-PET. Nucl. Instrum. Meth. Phys. Res. A. 2006 Dec.vol. 569(no. 2):421–424.

17. Mullani N, Wong W, Hartz P, Philippe E, Yerian K. Sensitivity improvement of TOFPET by the utilization of the inter-slice coincidences. IEEE Trans. Nucl. Sci. 1982 Feb.vol. 29(no. 1):479–483.

18. Daube-Witherspoon ME, Muehllehner G. Treatment of axial data in three-dimensional PET. J. Nuc. Med. 1987; vol. 28:1717–1724.

19. Defrise M, Casey ME, Christian M, Conti M. Fourier rebinning of time-of-flight PET data. Phys. Med. Biol. 2005 Jun.vol. 50(no. 12):2749–2763. [PubMed: 15930600]

20. Vandenberghe S, Daube-Witherspoon ME, Lewitt RM, Karp JS. Fast reconstruction of 3D time-of-flight PET data by axial rebinning and transverse mashing. Phys. Med. Biol. 2006 Mar.vol. 51(no. 6):1603–1621. [PubMed: 16510966]

21. Defrise M, Panin V, Michel C, Casey ME. Continuous and discrete data rebinning in time-of-flight PET. IEEE Trans. Med. Imag. 2008 Sep.vol. 27(no. 9):1310–1322.

22. Defrise, M.; Panin, V.; Sureau, F.; Abella, M.; Casey, M. An exact axial rebinning method for time-of-flight PET; Proc. 10th Int. Meeting Fully 3D Imag. Recon. Rad. Nucl. Med; 2009. p. 335-338.

23. Cho S, Ahn S, Li Q, Leahy RM. Analytical properties of time-of-flight PET data. Phys. Med. Biol. 2008 Jun.vol. 53(no. 11):2809–2821. [PubMed: 18460746]

24. Cho S, Ahn S, Li Q, Leahy RM. Exact and approximate Fourier rebinning of PET data from time-of-flight to non time-of-flight. Phys. Med. Biol. 2009 Feb.vol. 54(no. 3):467–484. [PubMed: 19124956]

25. Defrise M, Kinahan PE, Townsend DW, Michel C, Sibomana M, Newport DF. Exact and approximate rebinning algorithms for 3-D PET data. IEEE Trans. Med. Imag. 1997 Apr.vol. 16(no. 2):145–158.

26. Liu X, Defrise M, Michel C, Sibomana M, Comtat C, Kinahan P, Townsend D. Exact rebinning methods for three-dimensional PET. IEEE Trans. Med. Imag. 1999 Aug.vol. 18(no. 8):657–664.

27. Ahn, S.; Cho, S.; Li, Q.; Leahy, RM. Optimized weighting for Fourier rebinning of three-dimensional time-of-flight PET data to non-time-of-flight; Proc. IEEE Nucl. Sci. Symp. Med. Imag. Conf; 2009. p. 2989-2996.

28. Groiselle CJ, Glick SJ. 3D PET list-mode iterative reconstruction using time-of-flight information. Proc. IEEE Nucl. Sci. Symp. Med. Imag. Conf. 2004; vol. 4:2633–2638.

29. Daube-Witherspoon ME, Surti S, Matej S, Werner M, Jayanthi S, Karp JS. Influence of time-of-flight kernel accuracy in TOF-PET reconstruction. Proc. IEEE Nucl. Sci. Symp. Med. Imag. Conf. 2006; vol. 3:1723–1727.

30. Watson CC. An improved weighting kernel for analytical time-of-flight PET reconstruction. IEEE Trans. Nucl. Sci. 2008 Oct.vol. 55(no. 5):2551–2556.

31. Stark, H.; Woods, JW. Probability, Random Processes, and Estimation Theory for Engineers. 2 ed.. Englewood Cliffs, NJ: Prentice-Hall; 1994.

32. Lehmann, EL.; Casella, G. Theory of Point Estimation. New York: Springer-Verlag; 1998.

33. Oppenheim, AV.; Schafer, RW.; Buck, JR. Discrete-Time Signal Processing. 2nd ed.. Upper Saddle River, NJ: Prentice-Hall; 1999.

34. Vunckx K, Zhou L, Matej S, Defrise M, Nuyts J. Fisher information-based evaluation of image quality for time-of-flight PET. IEEE Trans. Med. Imag. 2010 Feb.vol. 29(no. 2):311–321.

35. Liu X, Comtat C, Michel C, Kinahan P, Defrise M, Townsend D. Comparison of 3D reconstruction with OSEM and FORE+OSEM for PET. IEEE Trans. Med. Imag. 2001 Aug.vol. 20(no. 8):804–813.

36. Fessler JA. Penalized weighted least-squares image reconstruction for positron emission tomography. IEEE Trans. Med. Imag. 1994 Jun.vol. 13(no. 2):290–300.

37. Jakoby BW, Bercier Y, Watson CC, Rappoport V, Young J, Bendriem B, Townsend DW. Physical performance and clinical workflow of a new LSO HI-REZ PET/CT scanner. Proc. IEEE Nucl. Sci. Symp. Medical Imaging Conf. 2006; vol. 5:3130–3134.

38. Siddon RL. Fast calculation of the exact radiological path for a three-dimensional CT array. Med. Phys. 1985 Mar.vol. 12(no. 2):252–255. [PubMed: 4000088]

39. Segars, WP. Ph.D. dissertation. Univ. North Carolina: Chapel Hill; 2001. Development and application of the new dynamic NURBS-based cardiac-torso (NCAT) phantom.

40. Yavuz M, Fessler JA. Statistical image reconstruction methods for randoms-precorrected PET scans. Med. Imag. Anal. 1998 Dec.vol. 2(no. 4):369–378.

41. Qi J, Leahy RM, Hsu C, Farquhar TH, Cherry SR. Fully 3D bayesian image reconstruction for the ECAT EXACT HR+ IEEE Trans. Nucl. Sci. 1998 Jun.vol. 45(no. 3):1096–1103.

42. Hudson HM, Larkin RS. Accelerated image reconstruction using ordered subsets of projection data. IEEE Trans. Med. Imag. 1994 Dec.vol. 13(no. 4):601–609.

43. Qi J, Leahy RM. Resolution and noise properties MAP reconstruction for fully 3D PET. IEEE Trans. Med. Imag. 2000 May.vol. 19(no. 5):493–506.

44. Qi J, Leahy RM, Cherry SR, Chatziioannou A, Farquhar TH. High resolution 3D bayesian image reconstruction using the microPET small-animal scanner. Phys. Med. Biol. 1998 Apr.vol. 43(no. 4):1001–1014. [PubMed: 9572523]

45. Hayes, MH. Statistical Digital Signal Processing and Modeling. New York: Wiley; 1996.
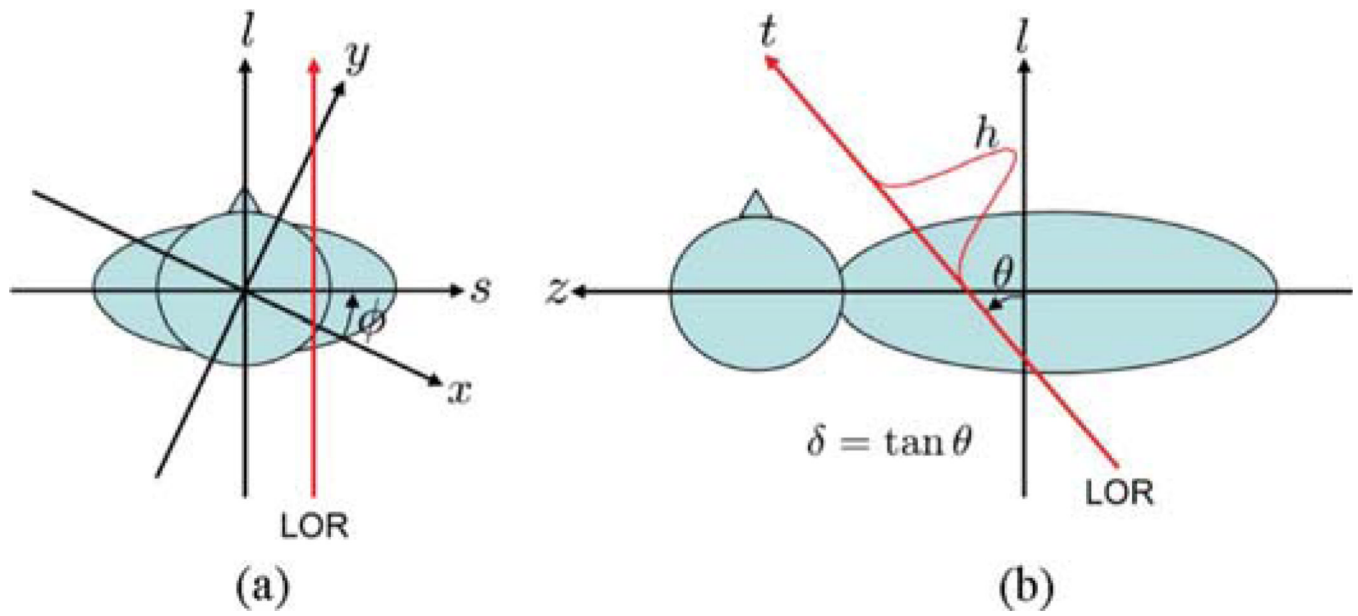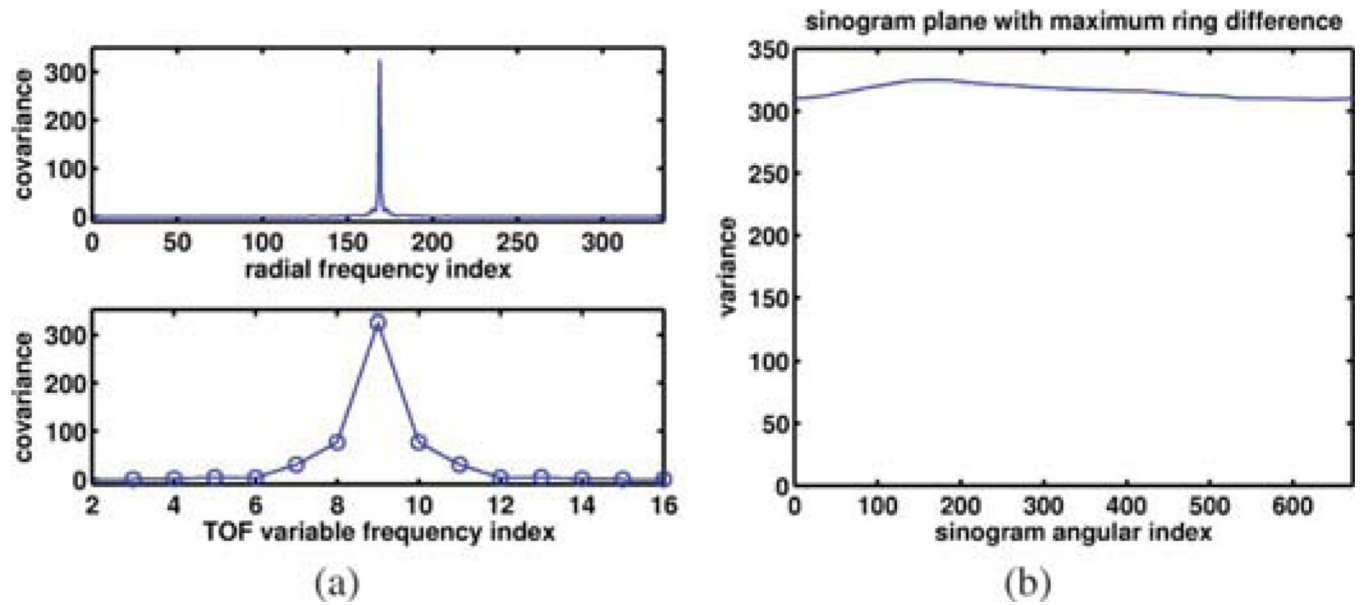
Fig. 1.
Data acquisition geometry: (left) transverse and (right) sagittal view. 3D TOF data are line integrals of a 3D object along an LOR weighted by a TOF kernel h. Each LOR is specified by s, ϕ, z, and $\delta = \tan\theta$.
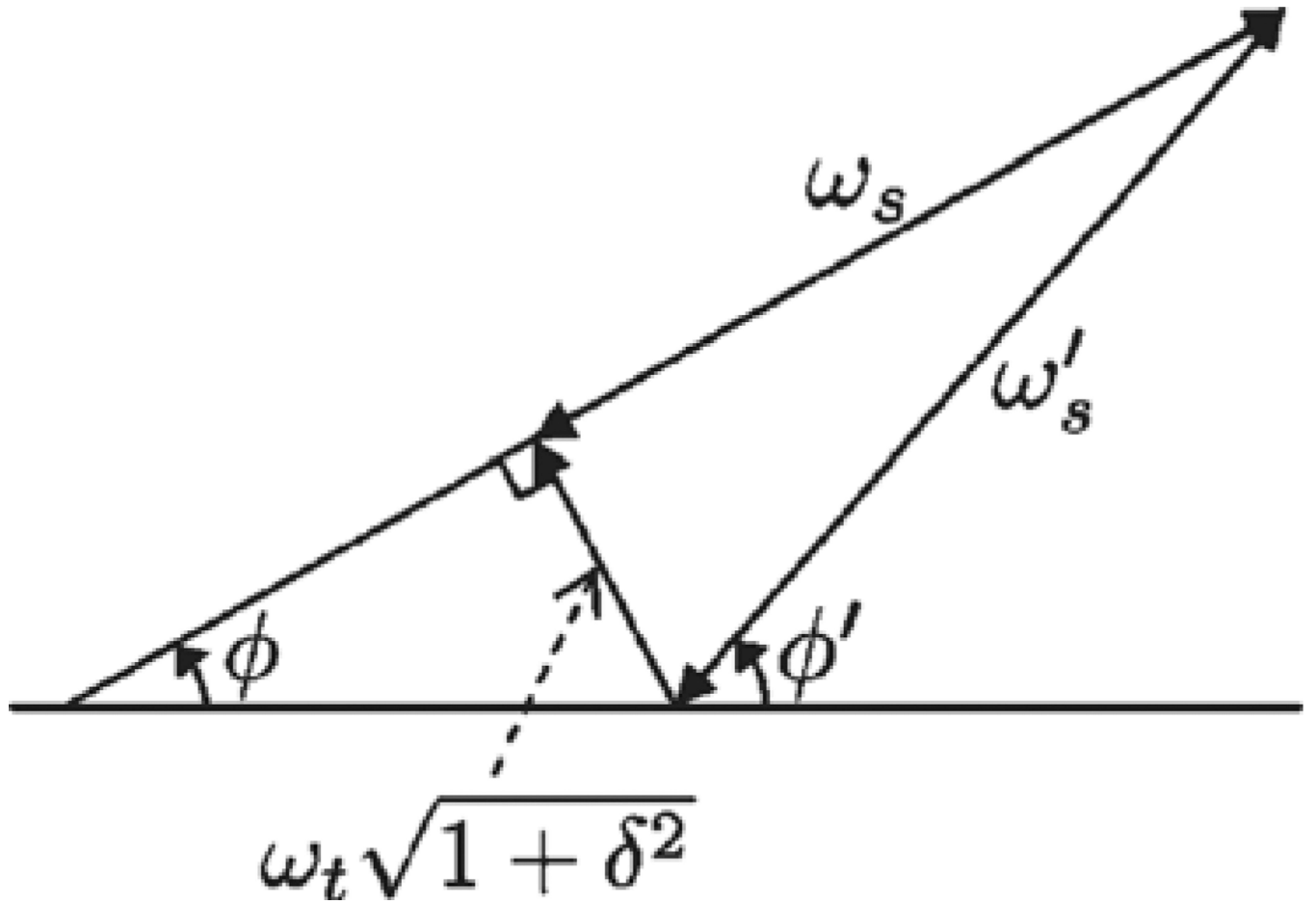
Fig. 2.
Geometric illustration of the coordinate transformation for the approximate mappings between a TOF oblique sinogram $\wp_{z,\delta,\omega_t}(\omega_s, \phi)$ and a non-TOF oblique sinogram $\wp'_{z,\delta}(\omega'_s, \phi')$.

Fig. 3.
Illustration of the noise properties of 3D TOF data in Fourier domain. (a) Covariance C_m^{ij} of the 2D FFT of the 3D TOF data with respect to the radial coordinate and the TOF variable index. This figure shows profiles along the radial frequency and the TOF frequency direction. In this figure, the zero-frequency component was shifted to the center. (b) Sum of the data variance over the radial and TOF variable index versus transaxial angular index for the oblique plane with the maximum ring difference.
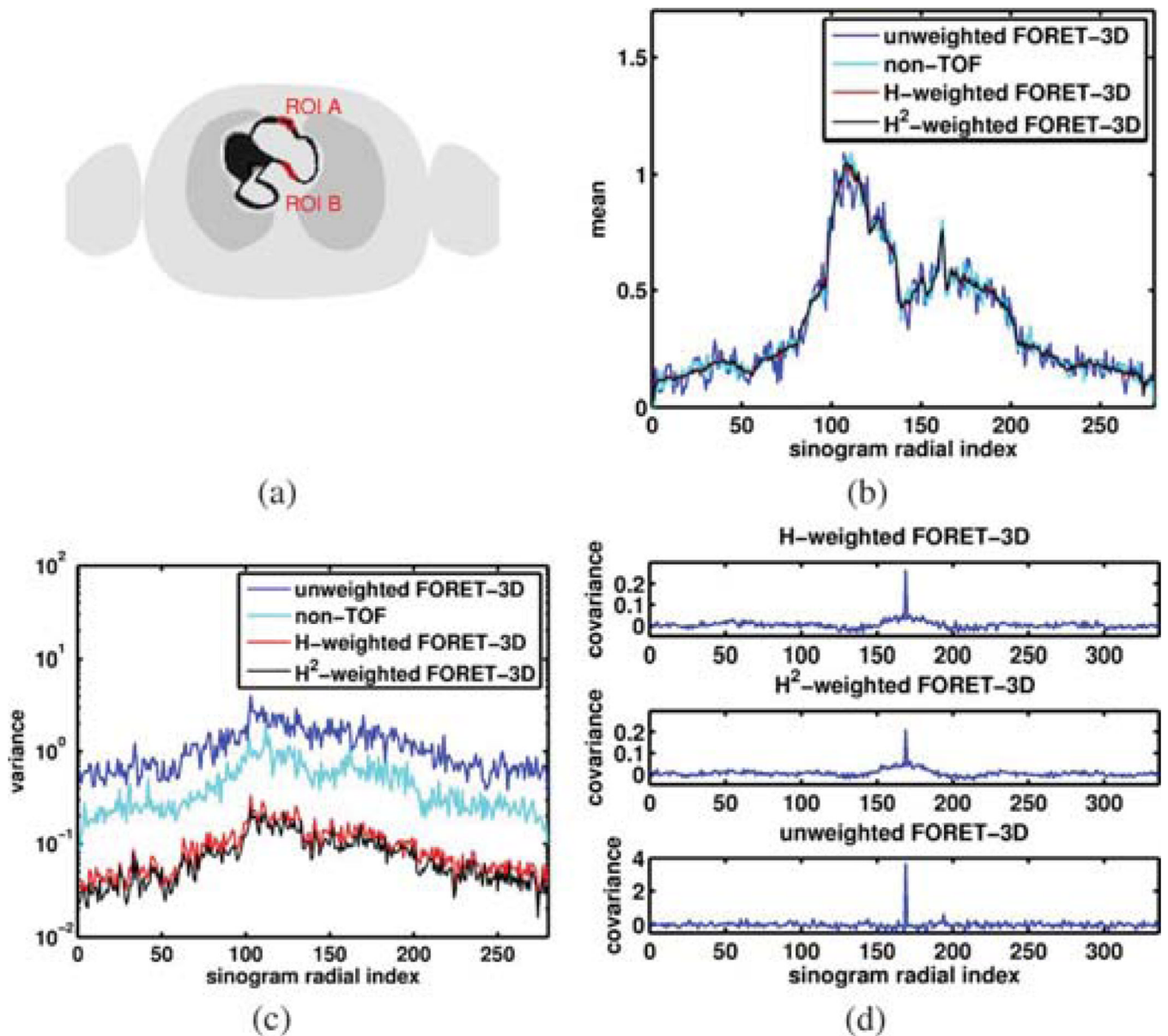
Fig. 4.
(a) Axial center plane of the NCAT torso phantom used for Monte Carlo simulation studies. Two ROIs are shown: ROI A with 36 voxels (144 mm^2) and ROI B with 23 voxels (92 mm^2). (b) Sample mean profiles and (c) sample variance profiles for the rebinned data and the non-TOF data acquired without TOF information in an axial center plane with the maximum ring difference. Note the variance profile in (c) is plotted on log scale. (d) Profiles of the covariance of the rebinned data. The covariance was calculated between a sinogram bin (radial index = 169, angular index= 169) and all other sinogram bins in the same oblique plane. For (b)–(d), the profiles were taken at the 169th angle corresponding to $\phi = \pi/2$.
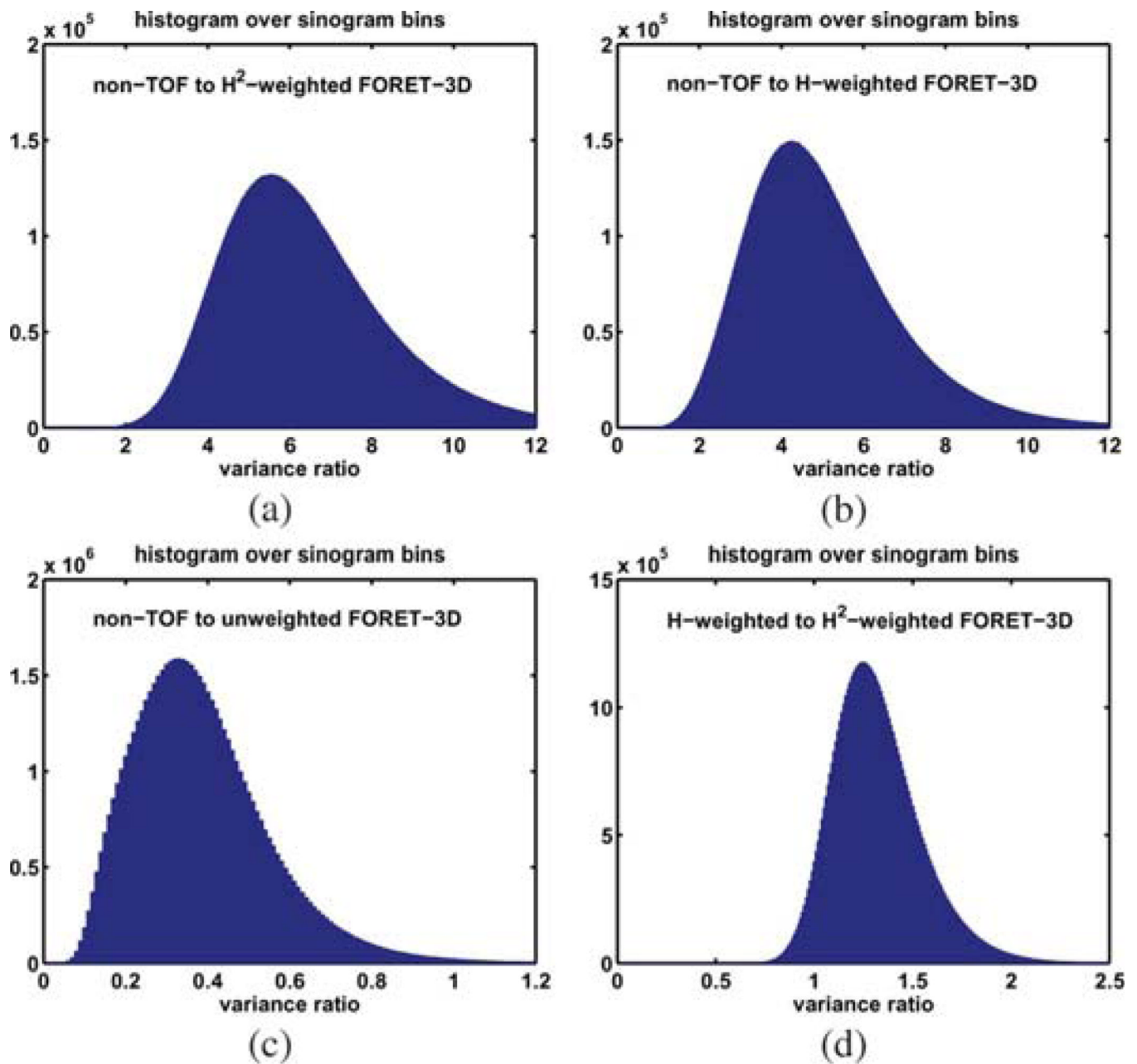
Fig. 5.
Histograms (over sinogram bins) of the ratios of the variance for the non-TOF data, acquired without TOF information, to that for (a) H^2-weighted FORET-3D, (b) H-weighted FORET-3D, and (c) unweighted FORET-3D. (d) Histogram of the ratios of the variance for H-weighted to H^2-weighted FORET-3D.
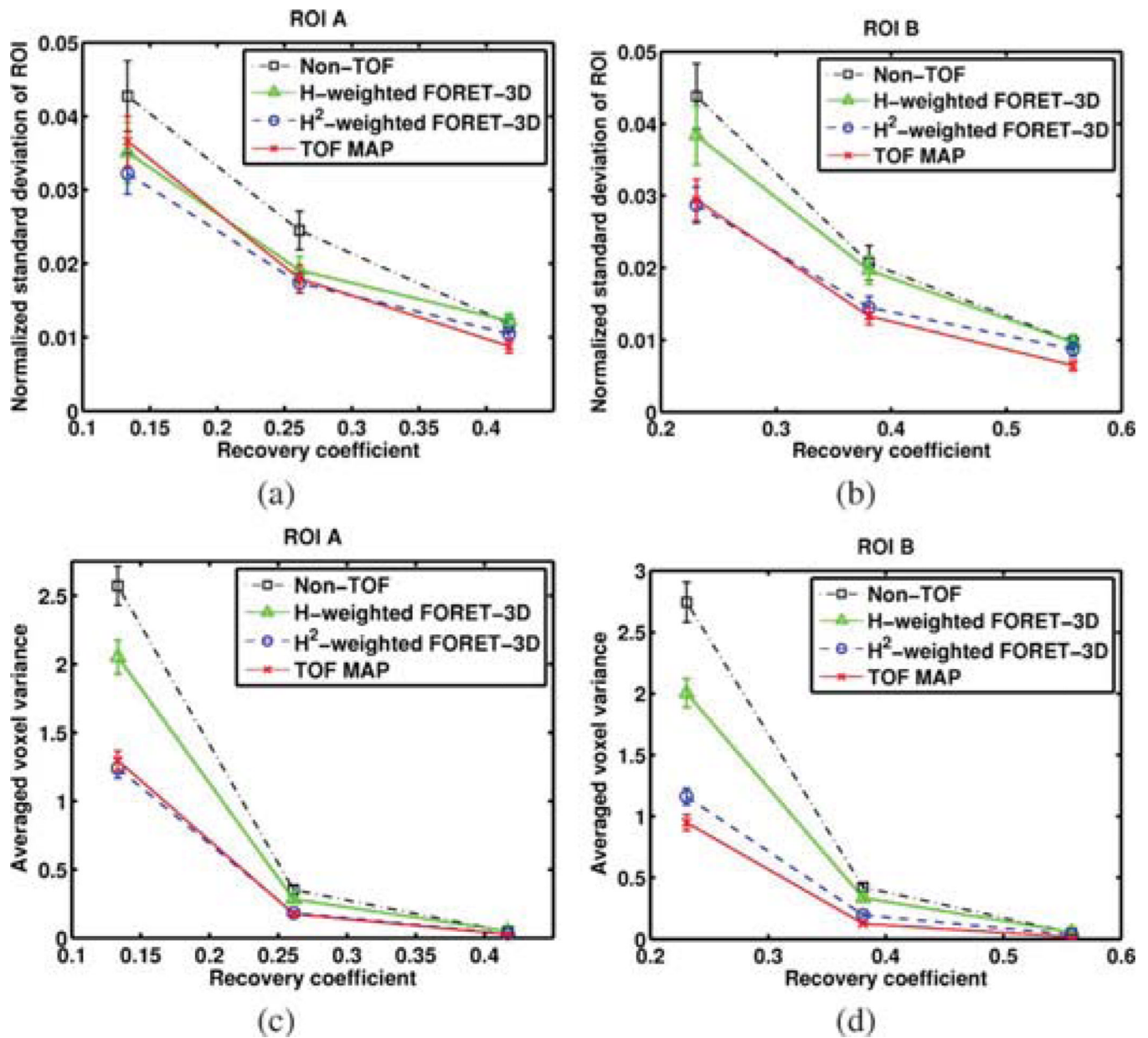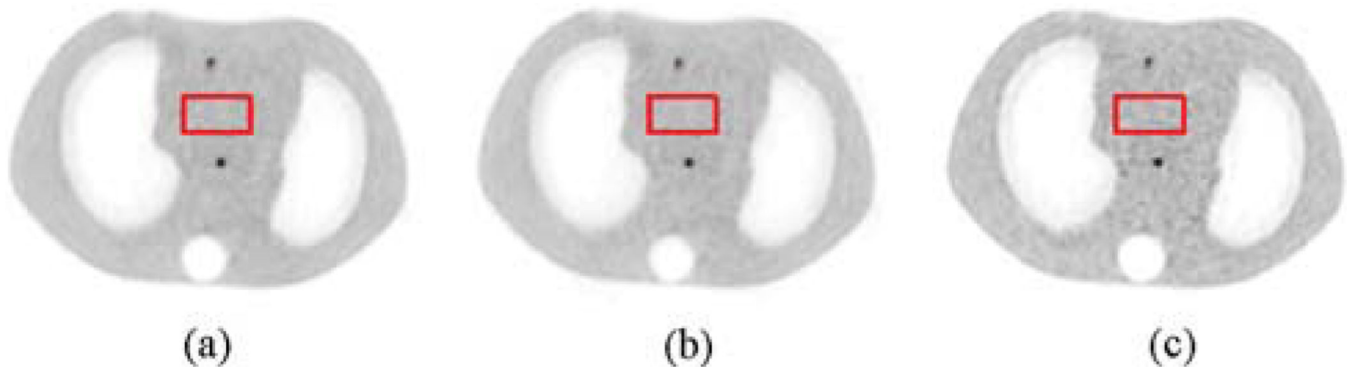
Fig. 6.
ROI recovery coefficient versus ROI standard deviation trade-off curves for ROI quantitation: (a) ROI A and (b) ROIB. ROI recovery coefficient versus voxel-wise variance across realizations with variances averaged within ROI: (c) ROI A and (d) ROI B. The error bars represent the standard errors estimated by a bootstrap method.

(a)   (b)   (c)

Fig. 7.
A transverse plane of fully 3D reconstructed images from the rebinned data by (left) H^2-weighted FORET-3D, (middle) H-weighted FORET-3D and (right) from the non-TOF data acquired without TOF information, using real phantom data. The red rectangle represents the background ROI used to calculate the contrast to noise ratio. A 4×4 voxel ROI that includes the lesion in the center was taken as a lesion ROI. Contrast-to-noise ratio (CNR) values were calculated as 17.97 for H^2-weighted FORET-3D (left), 16.41 for H-weighted FORET-3D (middle) and 10.95 for the non-TOF data acquisition (right).